A Molecular Movie at 1.8 Å Resolution Displays the Photocycle of Photoactive Yellow Protein, a Eubacterial Blue-Light Receptor, from Nanoseconds to Seconds†

Zhong Ren,*,‡,§,Δ Benjamin Perman,‡,|| Vukica Šrajer,‡,§ T.-Y. Teng,‡,§ Claude Pradervand,‡,§,⊥ Dominique Bourgeois,@,# Friederich Schotte,#,+ Thomas Ursby,#,O Remco Kort,▽,★ Michael Wulff,# and Keith Moffat*,‡,§,●

Department of Biochemistry and Molecular Biology, Consortium for Advanced Radiation Sources, and Institute for Biophysical Dynamics, The University of Chicago, 920 East 58th Street, Chicago, Illinois 60637, Institut de Biologie Structurale Jean-Pierre Ebel, UMR 9015, 41 Avenue Jules Horowitz, 38027 Grenoble Cedex 1, France, European Synchrotron Radiation Facility, BP 220, 38043 Grenoble Cedex, France, and Department of Microbiology, E. C. Slater Institute, BioCentrum, University of Amsterdam, Nieuwe Achtergracht 127, 1018 WS Amsterdam, The Netherlands

Received April 6, 2001; Revised Manuscript Received August 20, 2001

Ⓦ **This paper contains enhanced objects available on the Internet at http://pubs.acs.org/biochemistry.**

ABSTRACT: The photocycle of the bacterial blue-light photoreceptor, photoactive yellow protein, was stimulated by illumination of single crystals by a 7 ns laser pulse. The molecular events were recorded at high resolution by time-resolved X-ray Laue diffraction as they evolved in real time, from 1 ns to seconds after the laser pulse. The complex structural changes during the photocycle at ambient temperature are displayed in a movie of difference electron density maps relative to the dark state. The step critical to entry into the photocycle is identified as flipping of the carbonyl group of the 4-hydroxycinnamic acid chromophore into an adjacent, hydrophobic environment rather than the concomitant isomerization about the double bond of the chromophore tail. The structural perturbation generated at the chromophore propagates throughout the entire protein as a light-induced "protein quake" with its "epicenter" at the carbonyl moiety of the chromophore.

Photoactive yellow protein (PYP,[1] *1*) from the photoautotrophic purple eubacterium *Ectothiorhodospira halophila* is a 14 kDa, water-soluble, cytoplasmic blue-light receptor, in which a 4-hydroxycinnamic acid chromophore is covalently linked by a thioester bond to the γ-sulfur of Cys69 (*2*, *3*). Since the visible absorption spectrum of PYP with a maximum at 446 nm roughly matches the action spectrum of *E. halophila* for negative phototaxis (*4*), PYP is proposed to be the primary photoreceptor for this biological process. PYP also serves as the structural prototype (*5*) for the widely distributed Per-Arnt-Sim (PAS) domain class of signal transduction proteins (*6*). The 1.4 Å crystal structure [*7*; Protein Data Bank (PDB) entry 2phy] of the resting, dark state of PYP (denoted pG) showed that the chromophore of PYP is completely buried in a hydrophobic pocket with no atom exposed to solvent. The chromophore is stabilized in the trans configuration (Figures 1 and 2c) as the phenolate anion (*3*, *8*), in which the phenolate oxygen (O_4') is H-bonded to Tyr42 and the protonated side chain of Glu46 (*9*, *10*). Upon absorption of light by the pG state, PYP enters a fully reversible photocycle (Figure 2b) with a quantum yield of 0.35 (*11*). The photocycle in solution at room temperature is characterized by a set of short-lived, spectroscopically distinct intermediate states (Figure 2b) denoted P*, I_0, $I_0^{\ddagger}$, I_1 (or pR), and I_2 (or pB). The last is presumed to be the signaling intermediate whose conformation is sensed by unidentified downstream partner(s). Fourier transform in-

† Supported by NIH Grants GM36452 and RR07707 to K.M.

* To whom correspondence and reprint requests should be addressed. Z.R.: phone, (773) 702-3603; fax, (773) 702-0439; e-mail, renz@cars.uchicago.edu. K.M.: phone, (773) 702-2116; fax, (773) 702-0439; e-mail, moffat@cars.uchicago.edu.

‡ Department of Biochemistry and Molecular Biology, The University of Chicago.

§ Consortium for Advanced Radiation Sources, The University of Chicago.

Δ Present address: Renz Research, Inc., 1570 Wicke Ave., Des Plaines, IL 60018.

|| Present address: Department of Biophysics and Biophysical Chemistry, Johns Hopkins School of Medicine, Baltimore, MD 21205.

⊥ Present address: Swiss Light Source, Paul Scherrer Institut, CH-5232 Villigen PSI, Switzerland.

@ European Synchrotron Radiation Facility.

Present address: European Synchrotron Radiation Facility and LCCP IBS, UMR 9015, 41 Avenue Jules Horowitz, 38027 Grenoble Cedex 1, France.

+ Present address: NIDDK, National Institutes of Health, Building 5, Bethesda, MD 20892.

O Present address: MAX-lab, Lund University, P.O. Box 118, S-221 00 Lund, Sweden.

▽ University of Amsterdam.

★ Present address: Laboratory of Bioenergetics and Biophysics, Graduate School of Materials Science, Nara Institute of Science and Technology, Ikoma, Nara 630-0101, Japan.

● Institute for Biophysical Dynamics, The University of Chicago.

[1] Abbreviations: CCD, charge-coupled device; ESRF, European Synchrotron Radiation Facility; FTIR, Fourier transform infrared spectroscopy; GFP, green fluorescence protein; INS, isomorphous noise suppression; NSLS, National Synchrotron Light Source; PAS, Per-Arnt-Sim domain; PDB, Protein Data Bank; PYP, photoactive yellow protein; S/N, signal-to-noise ratio.

10.1021/bi0107142 CCC: $20.00
Published on Web 10/23/2001

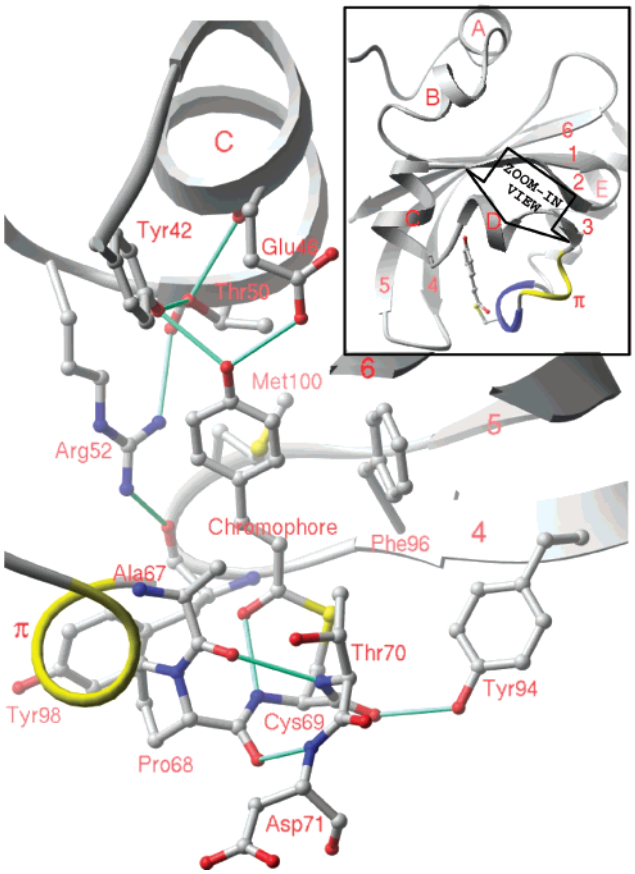

FIGURE 1: Chromophore binding pocket of PYP in the dark state [structure 2phy (*7*)]. The inset is a ribbon representation of the entire PYP molecule. α-Helices, β-strands, and loops are shown in gray, and the π-helix is shown in yellow. The two overlapping type III turns where the chromophore attaches to the protein are rendered in blue. Helices are labeled with letters and β-strands with numbers. Carbon atoms are rendered in gray, oxygens in red, nitrogens in blue, and sulfurs in yellow. Individual H-bonds in the principal H-bond network are depicted as thinner light green rods. All molecular graphics in Figures 1, 3, and 4, and the movie were made by using the software RIBBONS (*49*).

frared spectroscopy (FTIR; *9*, *10*) and time-resolved crystallographic experiments with 10 ms time resolution (*12*; PDB entry 2pyp) showed that in the I_2 state the chromophore has isomerized to the cis configuration (*13*), the H-bond to Glu46 is broken, O_4' of the chromophore acquires a proton either from the carboxyl group of Glu46 (*9*, *10*) or from solvent, and the guanidinium group of Arg52 that forms a lid on the chromophore pocket in the dark state swings away from the chromophore and partially exposes it to solvent (*12*).

Spectroscopic studies largely probe the electronic and vibrational structure of the chromophore and its immediate environment, and provide structural information only by inference. Our goal is to examine the structural changes associated with the photocycle directly: how they originate at the chromophore, propagate through the protein, and generate structural signals, in real time.

The recent development of techniques for ultrafast time-resolved X-ray crystallography has made direct structural analysis of short-lived intermediates at near-physiological temperature possible (*14*, *15*). We present here a set of time-dependent crystallographic measurements at ambient temperature obtained during the photocycle of PYP over nine decades in time, from 1 ns to 5 s after initiation of the photocycle (Figure 2a) by illumination of the crystal with a 7 ns laser pulse. The measurements yield difference electron density maps that display the average difference in electron density between time *t* after initiation of the photocycle and time 0, the dark state pG. These time-dependent differences turn out to be small in magnitude and complex, to extend eventually over most of the protein, and to arise from the superposition of time-dependent populations of time-independent, intermediate structures. We find that there is not an exact parallelism between the spectroscopic and structural changes (see the Results and Discussion), and a mechanism based on one may not apply directly to the other. Structural refinement against time-resolved crystallographic data therefore requires identification of the structure-based, chemical kinetic mechanism and deconvolution of the structure factor set for each candidate intermediate structure from the measured structure factor sets (*16*). This constitutes the final goal of a time-resolved structural analysis, and is in progress for PYP (Z. Ren, K. Moffat, M. Schmidt, S. Anderson, S. Rajagopal et al., unpublished results). Nevertheless, important information about the overall time course of the structural changes can be derived from careful inspection of these difference electron density maps. We present this intermediate stage of the analysis here.

MATERIALS AND METHODS

Time-Resolved Experiments. Apo-PYP was expressed as an exogenous product of *Escherichia coli* (*3*, *17*) and reconstituted with the chromophore to yield holo-PYP (*18*), and then crystallized as described by McRee et al. (*19*). The crystals were nearly identical to those used by Borgstahl et al. (*7*) in space group $P6_3$ with the following cell constants: $a = b = 66.9$ Å and $c = 40.8$ Å. The protein is active and maintains its fully reversible photocycle in the crystal as shown by optical measurement. The rate constant associated with recovery of the characteristic 446 nm band of the dark state after stimulation by a pulsed laser was 2.6 ± 0.4 s^{-1} (380 ms) at 283 K (data not shown). Time-resolved Laue diffraction experiments of the pump−probe type were carried out on the ID09 station (*20*) of the European Synchrotron Radiation Facility (ESRF, Grenoble, France). Small crystals of PYP (80 μm × 80 μm × 150 μm) were excited at 288 K using a single laser pulse (1.5 to 2.5 mJ total pulse energy, 7 ns full width at half-maximum, 12 ns from baseline to baseline, 1.5 mm diameter beam at the crystal, and 495 nm wavelength) from a Coumarin 500 dye laser pumped by the third harmonic of a Nd:YAG laser (Continuum NY61-10/ND60). Tandem insertion device X-ray sources, a 43-pole wiggler and a hybrid 71-pole undulator delivering a usable wavelength range from 0.3 to 1.8 Å, were used simultaneously to further enhance the X-ray intensity at the crystal during operation of the storage ring in single-bunch mode at a low current of 15 mA. Structural changes were probed at a series of eight time delays after the 7 ns laser pulse, ranging from 1 ns to 1 ms (Figure 2a). The time from the peak of the laser pulse to the leading edge of the X-ray pulse or pulse train was controlled during the experiment (*21*). The time delay *t* is defined as the pulse center-to-center time. A single-bunch X-ray pulse was used for time delays of <1 μs; the 1.8 μs pulse train ($^2/_3$-filling super bunch) was used for longer time delays. The 7 ms (2−12 ms) time point recorded (*12*) at the X26C station of the National Synchrotron

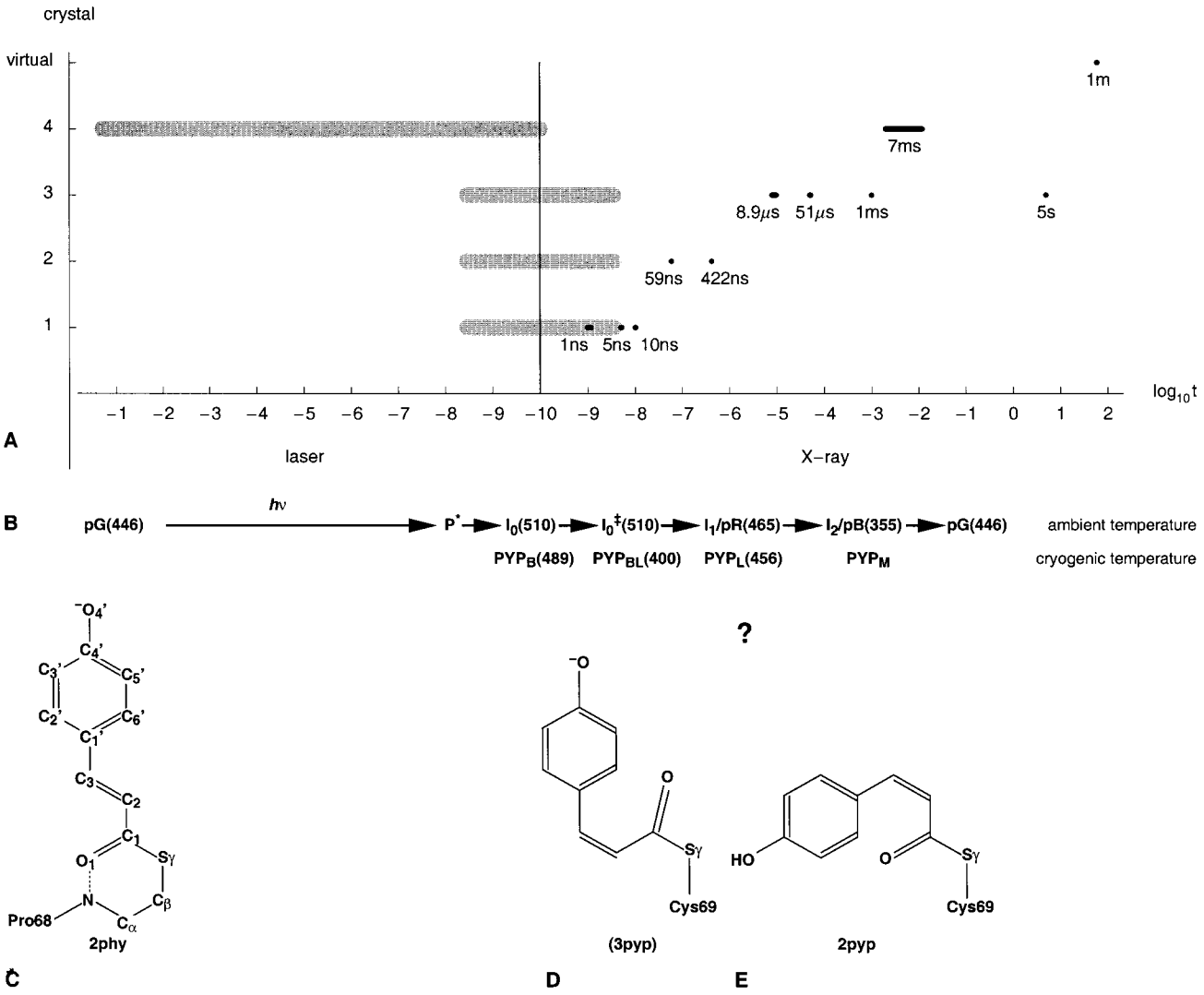

FIGURE 2: (a) Timing of laser and X-ray pulses. (b) Schematic drawing of the PYP photocycle. Symbols denote various spectroscopic intermediate states at ambient temperature, and are placed roughly according to the time at which they are maximally populated. Spectroscopic intermediate states at cryogenic temperatures are also shown. Absorption maxima (nanometers) are in parentheses. In aqueous solution at neutral pH, relaxation occurs from the initial excited electronic state (denoted P*) to short-lived intermediates (I_0 and $I_0^‡$; *50*, *51*). Further thermal relaxation to the next spectrally distinct intermediate state I_1 (also named pR) occurs within 10 ns. The system subsequently relaxes into a relatively long-lived, presumed signaling intermediate denoted I_2 (also named pB), maximally occupied 1 ms after photon absorption. The photocycle is completed by full recovery of the dark state pG in a few seconds (*30*, *32*). Only limited spectroscopic data are available on the photocycle in the crystalline state (*31*, *34*; see also Materials and Methods). (c−e) Chromophore configurations of pG, $I_0^‡$/PYP_{BL}, and I_2/pB states, respectively. The "?" refers to an unknown chromophore configuration at the pR state. The PDB entry from which the configuration was observed is labeled at the bottom of each panel, except that 3pyp (in parentheses) presents a transition state-like configuration between trans and cis. Atoms are identified in panel c.

Light Source (NSLS, Brookhaven National Laboratory, Upton, NY) is also marked in Figure 2a as crystal 4. In this experiment, the 200 ms laser pulse from a CW Ar-ion laser tuned to 495 nm was used to establish a photostationary state, and the end of the laser illumination is time 0. A virtual time point at 1 min, in which all difference structure factors are equal to 0, was added to restrain the exponential fittings. In the single-bunch experiments, 10 Laue images were accumulated on an image-intensified CCD detector prior to readout, for a single orientation of the crystal. The crystal orientation was then varied in 2° steps through a 60° angular range, to ensure highly redundant and complete coverage of reciprocal space. Each image was also recorded in an identical position but without the laser pulse, to obtain diffraction from the dark state, pG. Since dark measurements were recorded 5 s after the laser pulse of the previous angular setting, the data can be used as an additional time delay. Structure factor amplitudes were extracted from the Laue intensities using the *LaueView* suite (*22*, *23*).

Weighting of Difference Structure Factor Amplitudes. The Bayesian weight *w* applied to the difference structure factor amplitudes is based on that of Ursby et al. (*24*):

$$w = \frac{1}{1 + \dfrac{\Delta F^2}{\langle |\Delta F| \rangle^2} + \dfrac{{\sigma_{\Delta F}}^2}{\langle \sigma_{\Delta F} \rangle^2}} \qquad (1)$$

where ΔF is the difference of the structure factor amplitudes between time *t* and the dark state time 0, $|F_t| - |F_d|$. The values of $|F_t|$ and $|F_d|$ were derived from the same crystal wherever possible to minimize systematic errors arising from

Table 1: Crystallographic Data Statistics

	1	1	1	1	2	2	2	3[a]	3	3	3	4 (*12*)	4 (*12*)	$B_1 - B_6$[b]
laser to X-ray delay *t*	dark	1 ns	5 ns	10 ns	dark	59 ns	422 ns	dark (5 s)	8.9 μs	51 μs	1 ms	dark	7 ms	−
laser pulse energy (mJ)	−	2.5	2.5	2.5	−	2.5	2.5	(2.2)	2.2	2.2	1.5	−	−	−
extent of photo-initiation ϵ	−	1	1	1.25	−	1.75	1.75	(1.75)	1.75	1.75	0.75	−	2.5	1
Single Reflections														
no. of observations	190053	182155	164454	160186	164787	134175	126801	126277	102819	100710	124992	64367	56947	−
no. of unique reflections[c]	13379	13027	13274	13223	12975	11475	11403	11627	10421	10410	11694	10552	10354	−
overall redundancy	14.2	14.0	12.4	12.1	12.7	11.7	11.1	10.8	9.9	9.7	10.7	6.1	5.5	−
R_{merge} on F^2 (%)[d]	10.9	10.7	11.1	11.2	10.6	12.5	12.6	10.3	10.2	10.3	10.4	11.8	12.5	−
R_{merge} on $\|F\|$ (%)[e]	4.3	4.2	4.3	4.3	4.1	4.7	4.7	4.0	3.8	3.8	4.1	8.8	9.4	−
Single and Harmonic Reflections														
no. of unique reflections[c]	14032	13970	14273	14256	11811	12306	12190	12460	11145	11137	12454	10724	10414	6081
Completeness (% by shell/cumulative)[g]														
resolution range (Å)[f]														
∞−3.2	87.2	87.2	87.9	88.2	74.5	90.8	90.9	91.1	92.2	93.4	90.9	93.5	94.1	67.8
3.2−1.8	91.9	92.0	91.8	91.9	91.9	95.2	95.1	96.4	94.4	94.3	96.	90.5	89.3	62.3
	91.1	91.1	91.1	91.2	88.8	94.4	94.3	95.5	94.2	94.1	|95.3	91.0	90.2	63.3
1.8−1.6	83.4	84.2	85.5	85.5	86.4	71.6	69.4	72.5	46.4	46.3	72.8	44.4	41.6	−
	88.8	89.1	89.4	89.5	84.9	87.6	86.9	88.6	80.0	79.9	88.7	77.2	75.8	
R_{scale} (%)[h]	−	14	12	14	−	15	16	(8.7)	18	18	15	−	10	−

[a] The dark data set from crystal 3 was also used as a 5 s time point, since the dark data were collected 5 s after the previous laser illumination. This time point also provides an estimate for the internal noise level of our data collection and processing procedures. Related statistics are in parentheses. [b] Complex coefficient sets from reciprocal space fitting. Only those common reflections throughout all measured data sets up to 1.8 Å resolution are retained. [c] Unique reflections where $|F|/\sigma_{|F|} > 2$, where $\sigma_{|F|}$ is the root-mean-square deviation determined from merging all structure factor amplitudes $|F|$. [d] $R_{merge} = \sum|F^2 - \langle F^2\rangle|/\sum F^2$, where $\langle F^2\rangle$ is the mean of multiple observations and symmetry-related measurements. [e] $R_{merge} = \sum||F| - \langle|F|\rangle|/\sum|F|$. [f] All data were integrated to 1.6 Å resolution, and wavelength normalization (*23*) was conducted to 1.6 Å resolution; however, only data to 1.8 Å resolution were used to calculate difference maps. [g] Completeness by resolution shells for singles and multiples combined. Cumulative completeness is also shown after the bar. [h] $R_{scale} = \sum|S|F_t| - |F_d||/\sum|F_d|$, where $|F_d|$ and $|F_t|$ are the observed structure factor amplitudes for the dark state and at time delay *t*, respectively, and *S* is a scale factor. If available, the dark data set from the same crystal was used, but if not, the dark data set from crystal 1 was used.

crystal-to-crystal variation. $\sigma_{\Delta F}^2$ is the variance of ΔF, the summation of the variances of $|F_t|$ and $|F_d|$. The symbol $\langle x\rangle$ denotes the mean of all values of *x*.

Isomorphous Noise Suppression. Isomorphous noise suppression is a difference density modification procedure developed to enhance the signal-to-noise ratio (S/N) in difference electron density maps (Z. Ren et al., unpublished results). The INS procedure derives phase information for the structure factor difference, and is directly analogous to well-established density modification procedures (*25*) such as solvent flattening more commonly applied to Fourier maps. The theory that underlies the phase improvement by (difference) density modification is presented elsewhere (*25*). The level of density suppression should be proportional to the probability that a difference density value is due to noise. Difference electron densities were not altered if they lie within 4 Å of any chromophore atom or of protein atoms from residues 42, 46, 50, 52, 65−73, and 96, in the 2phy or 2pyp models. Densities were reduced to 62% of their initial values if they lie within 4 Å of any atoms of residues 37−85 and 94−105 (but not if they lie near any atom on the previous list), comprising β-strand 2, helices C, D, π, and E, and part of β-strands 3 and 4. All densities in the rest of the protein were reduced to 38% of their initial values. All difference density values in the solvent region, no closer than 4 Å to any atom of the protein or chromophore in both 2phy and 2pyp, were set to 0. The modified map was inverse-transformed to yield difference Fourier coefficients and phases (see the Supporting Information). The INS procedure results in a new phase set for difference Fourier synthesis that is completely uncorrelated with the original phase set. The procedure was iterated to convergence, which required four or fewer cycles.

RESULTS AND DISCUSSION

Improved Difference Maps Reveal Snapshots of the PYP Photocycle. The data set obtained at each time delay after photoinitiation of the PYP photocycle (Table 1) was first analyzed independently. Structure factor amplitudes from single and multiple Laue spots were combined (*23*) and scaled to the structure factor amplitudes calculated from the atomic structure of the dark state pG (*7*). Standard, unweighted difference Fourier maps were calculated (*26*) with phases derived from the 2phy model of the pG state, in which all atoms of the chromophore and of residues 42, 46, 50, 52, and 65−73 were omitted from the phase calculation (Figure 3a). Although these maps show some crystallographically significant and chemically plausible features at and near the chromophore, their S/N is poor. The signal is diminished by the relatively low extent of photoinitiation in the crystals and by the small magnitude of the initial structural changes (*12*, *26*). The noise derives both from

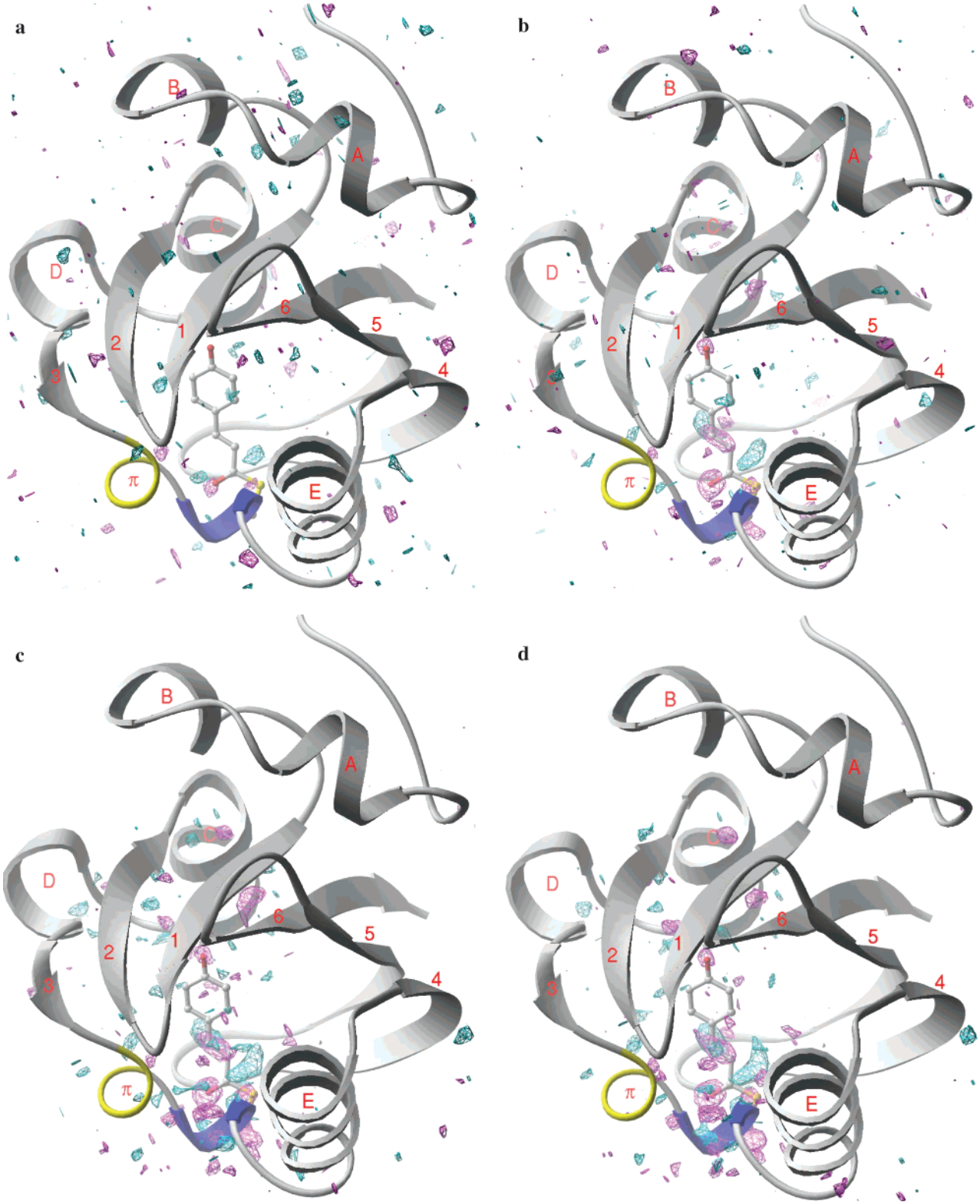

FIGURE 3: Difference electron density maps with a 1 ns delay. Negative and positive difference densities are in magenta and cyan, respectively. See the legend of Figure 1 for color coding of ribbons and atoms. Unweighted (a), weighted (b), INS-modified (c), and exponentially fitted (d) maps are contoured at $\pm 3.0\sigma$, $\pm 3.1\sigma$, $\pm 4.0\sigma$, and $\pm 3.8\sigma$, respectively, where σ is the standard deviation of the entire map.

errors in the two structure factor amplitudes and from the phase approximation inherent in such difference maps, in which the phase of the native structure factor (here, that of the dark state structure) is used in place of the true phase of the structure factor difference (*27*). Maps calculated using weighted difference amplitudes in which the weights are based on Bayesian statistics show greatly improved S/N's (compare panels b and a of Figure 3), and provide a clearer structural interpretation. To address the phase error, a new isomorphous noise suppression (INS) procedure was developed. After application of the INS procedure, the maps exhibit a further improvement in their S/N's and enhanced

structural detail (compare Figures 3c and 4 with panels a and b of Figure 3).

In time-resolved crystallographic experiments, each snapshot at a fixed time delay after reaction initiation is likely to represent a mixture of structural states (*16*). Nevertheless, authentic structural features in a time-dependent set of difference maps must satisfy several criteria that enable the signal to be distinguished from noise (*52*). In particular, when a complete set of maps at several time delays is considered, authentic features persist from map to map, whereas noise tends to vary sharply.

Four prominent negative features around the dark state chromophore are nearly constant in both position and amplitude in all maps (Figure 4): on the carbonyl oxygen O_1, the phenolate oxygen O_4', the vinyl carbons C_2 and C_3 of the chromophore, and the γ-sulfur of Cys69 (Figure 2c). A group of negative features on the guanidinium group of the Arg52 side chain appears at 59 ns and persists. Negative features on the aryl moiety of the chromophore are largely absent in early maps but finally appear at 7 ms. Other negative features appear on the side chains of Tyr42, Glu46, Thr50, Cys69, and Met100, and the main chain carbonyl oxygens of Ala67 and Pro68 in various time ranges. There are two prominent positive features exclusively in the 1 ns map (Figure 4a): one on the opposite side of the chromophore from the carbonyl oxygen and coplanar with the chromophore (denoted α) and another near the vinyl but displaced by 1 Å from the chromophore plane, toward Met100 (denoted β). In the 5 ns map (Figure 4b), a large, C-shaped, positive feature with a radius of 2 Å is centered on the vinyl double bond and again coplanar with the chromophore (denoted α and γ). The amplitude of this feature diminishes progressively from 10 (Figure 4c) to 59 ns (Figure 4d).

We conclude that many prominent negative and positive features in the weighted and INS-enhanced difference maps (Figures 3b, 3c, and 4) have good temporal connectivity, which further validates them as authentic features.

Empirical Rates of Structural Changes in the PYP Photocycle. The snapshots of the PYP photocycle were then analyzed jointly to extract the time dependence of the structural signals in real space. The INS maps (Figure 4) were recalculated on a direct lattice grid ($72 \times 72 \times 54$ along the *a*, *b*, and *c* axes, respectively) coarser than that used for visualization. From these maps, 193 crystallographically independent grid points were selected, lying on the significant structural features noted above. A number of mathematical functions could in principle be used for the purpose of time smoothing, to represent the time dependence. For example, polynomial, exponential, or stretched exponential functions might be appropriate. Exponential functions arise naturally in describing the time-dependent population of species in a unimolecular chemical kinetic model (*28*). We chose initially to model the difference electron density values, $\Delta\rho(r_j,t)$, at these grid points r_j ($j = 1, 2, ..., 193$) as a sum of exponential functions of time delay *t*. Thus

$$\Delta\rho(r_j,t) = \epsilon\sum_i A_i(r_j)\exp(-k_i t) \qquad (2)$$

where $A_i(r_j)$ is the difference electron density for transient *i* at grid point r_j, k_i is the empirical rate for transient *i*, and ϵ is the relative extent of photoinitiation for a particular data set. Equation 2 is based on the key assumption that all points r_j in real space vary with the same set of empirical rates k_i, and thus, the space and time variables can be separated. Those grid points r_j at which $\Delta\rho$ does not vary significantly with a particular rate k_i will be associated with small values of the coefficients $A_i(r_j)$. The nonlinear least-squares fitting to eq 2 used a trust-region implementation of the Levenberg−Marquardt method (*29*; Z. Ren, R. Sheng, S. Wright, unpublished results). Due to the limited number of experimental time points available, only empirical rates differing by more than 1 order of magnitude could be reliably isolated. The initial values of ϵ were derived from the input laser pulse energy, the laser focal spot size, and the overall standard deviation of the difference electron densities, and subsequently refined on a trial-and-error basis (Table 1).

Since the 1 ns map (Figure 4a) is qualitatively different from the 5 and 10 ns maps (Figure 4b,c; see below), there must be a rate of $2-5 \times 10^8$ s^{-1} (time constant τ of 5−2 ns; roughly adjusted to $k_1 \approx 3 \times 10^8$ s^{-1}, $\tau_1 \approx 3$ ns). The rough consistency between the spectroscopic rate in solution for the $I_0^{\ddagger}$ to I_1 transition (Figure 2b legend) and the rate of structural variation shown in our 1, 5, and 10 ns maps suggests that these maps display the structural conversion from $I_0^{\ddagger}$ to I_1 at ambient temperature in the crystal. The intensity of the 7 ns laser pulse that initiates the photocycle is still near its peak at the 1 ns delay time, but has greatly diminished by 5 and 10 ns (Figure 2a). An intense 7 ns laser pulse provides a sufficient duration for the generation of a photostationary state among the short-lived, rapidly interconverting intermediates P*, I_0, $I_0^{\ddagger}$, and I_1, together with the pG (or a pG-like) state. The 1 ns map may differ from the 5 and 10 ns maps because the latter two display only thermal relaxation from the photostationary state largely represented in the former. The dominant spectroscopic species in this putative photostationary state is likely to be $I_0^{\ddagger}$.

No rates in the range of 10^7-10^4 s^{-1} (100 ns to 100 μs) were identified in the spectroscopic results (Figure 2b legend). However, during the time range from a few nanoseconds to nearly a millisecond in which I_1 is populated, significant conformation changes are occurring, as shown by the evolution of structural features in the maps from 5 ns to 51 μs (Figure 4b−g). Thus, the spectroscopic I_1 (or pR) state contains more than one structural intermediate. From the varying difference electron densities over this time range, we identified two more rates: $k_2 = 3 \times 10^7$ s^{-1} (33 ns) and $k_3 = 4 \times 10^5$ s^{-1} (2.5 μs). Evidently, these structural changes are spectroscopically silent in the visible wavelength range.

The spectroscopic I_1 state decays biexponentially to I_2 in solution (*30*), with 60% of the spectral amplitude at a rate of 4000 s^{-1} (250 μs) and 40% of 830 s^{-1} (1.2 ms). Although we do not have enough time points in this time region to cleanly isolate these rates, we identified a rate k_4 of 900 s^{-1} (1.1 ms) that matches one of the spectroscopic rates. Both the 1 and 7 ms maps (Figure 4h,i), but not the preceding 51 μs map (Figure 4g), clearly exhibit the structure 2pyp determined by millisecond time-resolved crystallography and associated with the I_2 state (compare panels h and i of Figure 4 with Figure 2 of ref *12*). A negative feature located on or near the γ-sulfur of Cys69 at 51 μs continuously shifts at 1 and 7 ms. These maps do not reveal simple relaxation to the dark state, which suggests that further structural changes are

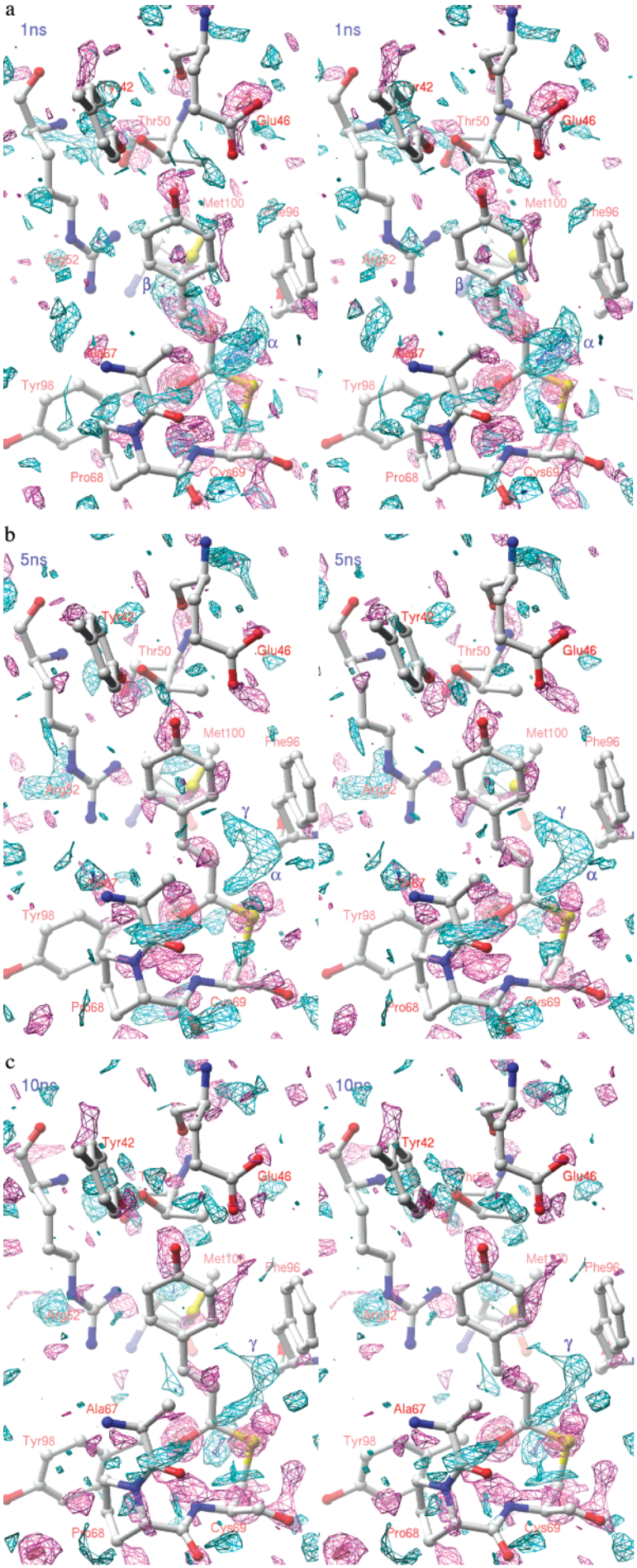
a
1ns
Tyr42
Thr50
Glu46
Met100
Phe96
Arg52
β
α
Ala67
Tyr98
Pro68
Cys69
1ns
b
5ns
Tyr42
Thr50
Glu46
Met100
Phe96
Arg52
γ
α
Ala67
Tyr98
Pro68
Cys69
5ns
c
10ns
Tyr42
Glu46
Met100
Phe96
Arg52
γ
Ala67
Tyr98
Pro68
Cys69
10ns

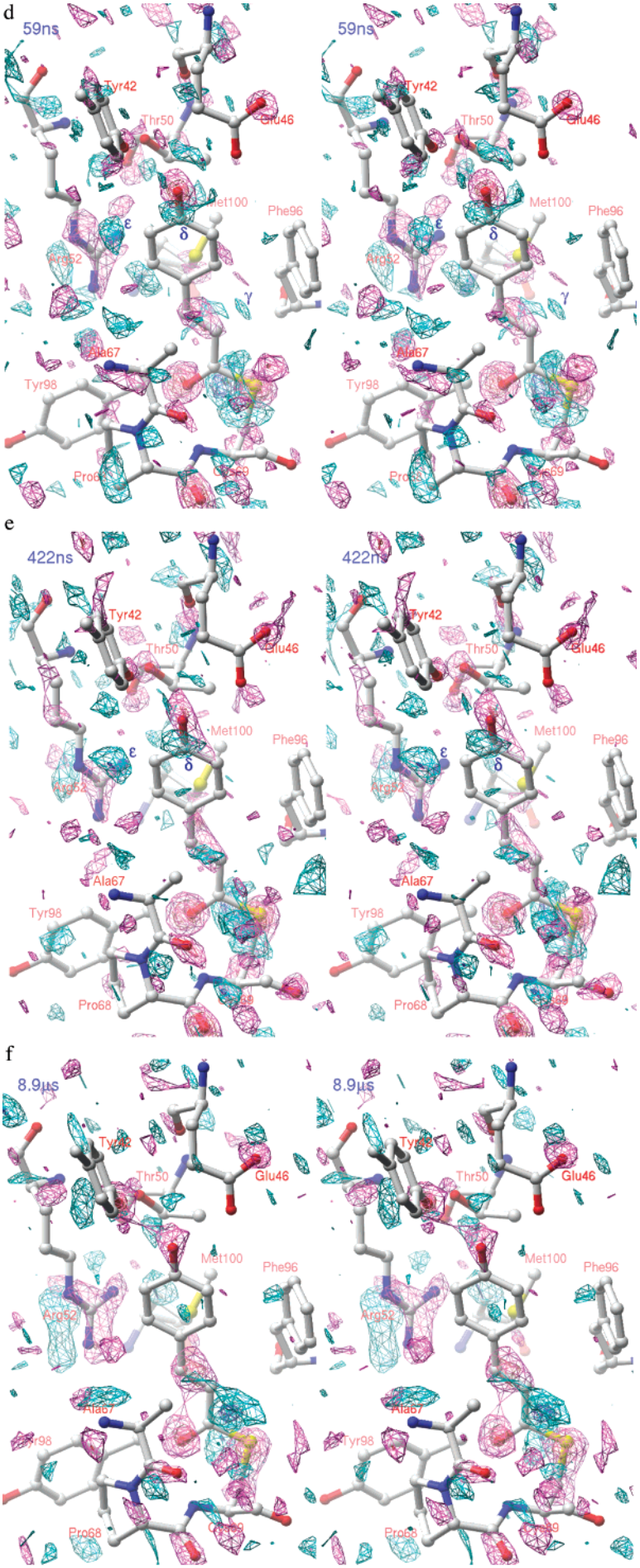
d
59ns
59ns
Tyr42
Thr50
Glu46
Met100
Phe96
Arg52
Ala67
Tyr98
Pro68
e
422ns
422ns
Tyr42
Thr50
Glu46
Met100
Phe96
Ala67
Tyr98
Pro68
f
8.9µs
8.9µs
Thr50
Glu46
Met100
Phe96
Arg52
Pro68

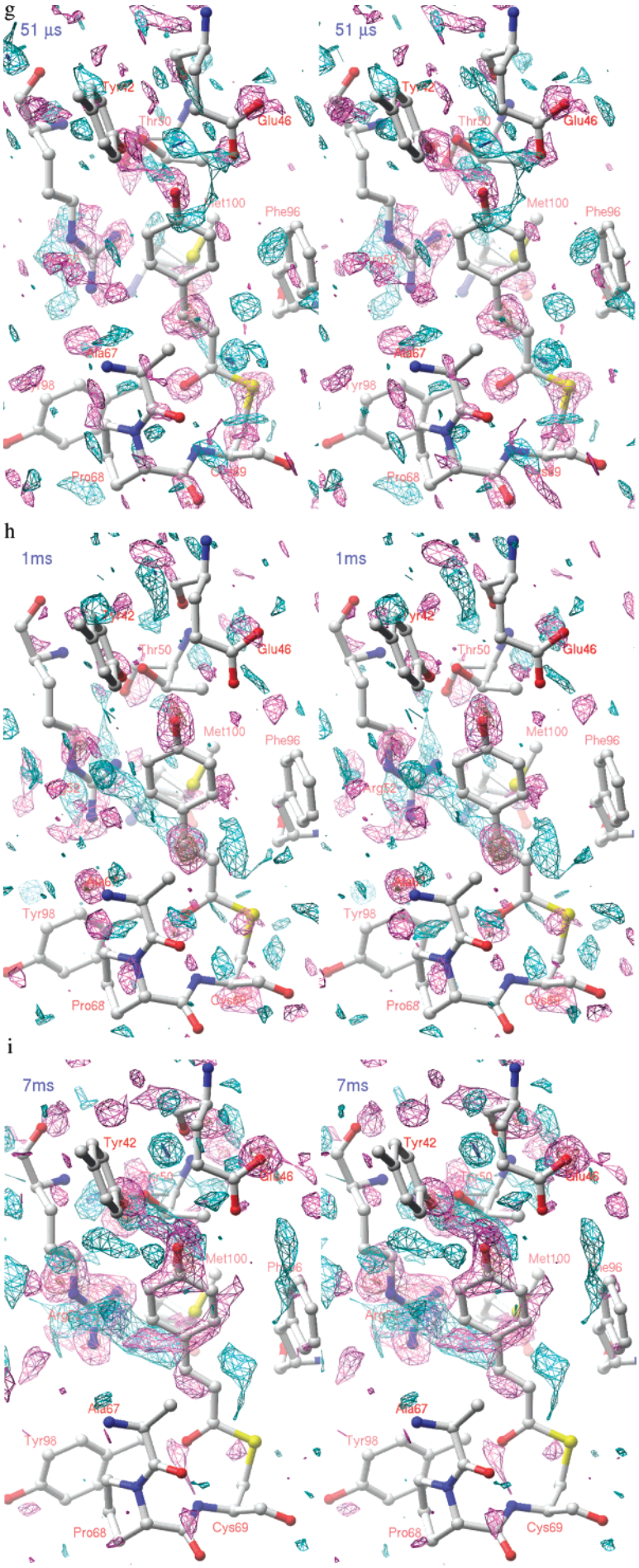
g
51 μs
Tyr42
Thr50
Glu46
Met100
Phe96
Ala67
Tyr98
Pro68
Cys69
51 μs
Tyr42
Thr50
Glu46
Met100
Phe96
Tyr98
Pro68
h
1ms
Tyr42
Thr50
Glu46
Met100
Phe96
Tyr98
Pro68
1ms
Tyr42
Thr50
Glu46
Met100
Phe96
Tyr98
Pro68
i
7ms
Tyr42
Met100
Ala67
Tyr98
Pro68
Cys69
7ms
Tyr42
Met100
Ala67
Tyr98
Pro68
Cys69

occurring at a rate at least 1 order of magnitude faster than the rate of the spectroscopically observed recovery of the dark state, which ranges from 6.7 (150 ms) to 0.5 s^{-1} (2 s; *30*, *31*; also see Materials and Methods). We infer a rate k_5 of ~50 s^{-1} (20 ms) based on these changes. We assigned a rate k_6 of ~1 s^{-1} (1 s) to the final relaxation from I_2 that recovers the dark state, based on our spectroscopic measurements on PYP crystals and rates reported from solution and crystal spectroscopic measurements (*30*−*32*). These six rates (k_1−k_6) were used to construct the molecular movie.

Photocycle "Movie". The real space fitting was largely restricted to significant features at the chromophore and its immediate environment, where the signals are concentrated in space. In contrast, the signal in reciprocal space, in which diffraction data are obtained, is distributed across all reflections. The noise on a given reflection in reciprocal space is considerably worse than at a given location in real space due to distribution of the signal in reciprocal space. Any time-dependent variation in real space must also be present in reciprocal space with the same mathematical form since these spaces are related by a Fourier transform, a linear process. The same algebraic form of eq 2 was therefore used to fit the time dependence of both the real and imaginary components of ΔF, the difference structure factor after four cycles of the INS procedure:

$$\Delta F(\mathbf{H},t) = \epsilon \sum_{i=1}^{6} B_i(\mathbf{H}) \exp(-k_i t) \qquad (3)$$

where **H** represents the Miller indices (*h*, *k*, *l*) of a reflection and B_i is the complex coefficient of the exponential term *i*. This fitting in reciprocal space adjusts only $B_i(\mathbf{H})$, but maintains the rates k_i and the relative extents of photoinitiation ϵ obtained from the fitting in real space. Reciprocal space fitting thus yields six sets of complex coefficients B_i (i = 1, ..., 6). Each set retains an entry for **H** if data are present for **H** in all 11 time delays. A total of 6081 unique reflections to 1.8 Å resolution satisfied this criterion and were fit to eq 3 (Table 1) to yield $\Delta F(\mathbf{H},t)$ and its Fourier transformation $\Delta\rho(r,t)$ as continuous functions of time. "Time smoothing" is therefore achieved by fitting all structure factors against a set of continuous functions of time sharing a common set of rates, and diminishes the noise uncorrelated with time (Figure 3d). Appropriate animation software can display the fitted maps for any selected time series. It is convenient to display this "molecular movie" on a time base that is uniform in log *t*. The residual complex vectors in the fitting of eq 3 result in a set of "residual maps" in which no significant feature is present and the noise is randomly distributed in time and real space (data not shown). This result verifies that a sum of exponential functions (eq 2) adequately models the data. The molecular movie presents the PYP photocycle as a series of fitted difference maps that allow direct visualization of the atomic motions that occur as PYP traverses its photocycle, from the nanosecond to the second time domain. The movie retains all significant negative and positive features in the experimental INS maps, but removes rapidly fluctuating noise in the time domain. The presentation in movie form retains the information in a series of snapshots or static maps (for example, Figure 4) in the time domain, and aids the visualization of certain features.

Overall Structural Changes. Substantial structural changes at the chromophore itself, on the distal side (upper, near Glu46) of the chromophore pocket, and particularly on the proximal side (lower, near Cys69) are evident from the earliest time point and are associated with isomerization about the chromophore double bond and motion of the carbonyl moiety. Changes on the distal side are of moderate extent from 512 ns to 256 μs, when they become substantially more prominent and decay after ~4 ms. Those on the proximal side are extensive, largely constant from 64 ns to 256 μs, and persist from 512 μs to 1 ms, after which they decay markedly. The overall impression is of the immediate generation of structural changes at the chromophore and on the proximal side; a complex evolution of these structural changes in the nanosecond to microsecond time range; a "flow" of structural change toward the distal side with a marked diminution of structural changes on the proximal side, and a rearrangement of the chromophore in the 256 μs to millisecond time range; and completion of the photocycle with reversion to the dark state in the range of tens to hundreds of milliseconds.

Motion of the Carbonyl Oxygen. The refined structure of PDB entry 2pyr (*26*, *33*) was based on our earlier structural interpretation of a single time point, the unweighted, 1 ns map (Figure 3a). Examination of the present, significantly improved 1 ns map and of the data at many time points incorporated in the movie leads us to revise our interpretation. Our movie shows the carbonyl oxygen of the chromophore displaced from its original position, in which it forms an H-bond to the amide nitrogen of Cys69, from 1 ns until ~1 ms, after which it rebinds to this amide. However, the carbonyl oxygen stays for only a few nanoseconds in a flipped position on the opposite side of the chromophore from its position in the dark state, a position also observed in the freeze-trapped structure 3pyp (*34*). Double isomerization about the vinyl bond and the thioester linkage was proposed as the structural route for flipping the carbonyl oxygen, based on a strengthened H-bond between the protonated carboxyl of Glu46 and the phenolate of the chromophore shown by FTIR spectroscopic observations at 80 K (*9*). The new environment of the flipped carbonyl oxygen is formed by five aromatic groups, from Phe62, Phe75, Tyr94, Phe96, and the chromophore itself, that constitute a very hydrophobic cavity (*34*). On the basis of the rough match between crystallographically and spectroscopically derived relaxation rates noted above, we propose that the flip of the carbonyl oxygen is the structural feature characteristic of the $I_0^{\ddagger}$ spectral state (perhaps also I_0) and associated with the large red shift of its absorption maximum from 446 to 510 nm. A

FIGURE 4: Stereoviews of the INS difference electron density maps. Each map corresponds to the laser-to-X-ray delay time shown in the upper left corner, and is superimposed on the dark structure 2phy (*7*). The maps are contoured at $\pm 3\sigma$, $\pm 5\sigma$, and $\pm 7\sigma$, where σ is the standard deviation of the entire map. Negative and positive difference densities are in magenta and red, and cyan and blue, respectively. See the legend of Figure 1 for color coding of atoms.

Ⓦ A molecular movie in GIF format is available. The rate constants used to construct this movie are 3×10^8, 3×10^7, 4×10^5, 900, 50, and 1 s^{-1}. The uncertainty of these rates is implied in the number of digits used.

noncovalent six-membered ring formed by the chromophore carbonyl group, the amide nitrogen, and the side chain of Cys69 (Figure 2c) is completely opened by flipping of the carbonyl moiety (Figure 2d). The strain thereby introduced into the tail of the chromophore would be expected to reduce the extent of charge delocalization from the phenolate oxygen through the aryl moiety to the tail and thus to produce a blue shift in the absorption maximum. However, insertion of the carbonyl oxygen between the two aromatic rings of Phe96 and the chromophore itself triggered motion of Phe96 away from the flipped carbonyl at cryogenic temperatures, as shown by extensive positive and negative features around Phe96 (see Figure 1c of ref *34*). In contrast, such features are essentially absent near Phe96 in our maps (Figures 3 and 4), at all time points. We therefore infer that the substantial red shift of $I_0^{\ddagger}$ is caused by the transiently established interaction between the flipped carbonyl and the aromatic moieties at ambient temperature, which is perturbed or absent at cryogenic temperatures.

Comparison between the difference map in Figure 1c of Genick et al. (*34*), our 5 ns map (Figure 4b), and the movie from 2 to 32 ns reveals a large positive density near aryl carbon C_6' (feature γ in Figure 4b) common to all maps. Other low-temperature experiments also show positive difference density at the same location (R. Kort, unpublished results). Its presence in several independent experiments suggests that it is an authentic signal. However, detailed comparison between results at ambient and cryogenic temperatures is hindered by the fact that the PYP photocycle takes a qualitatively different form at ambient and cryogenic temperatures. When motion of the chromophore and surrounding protein is greatly restricted at cryogenic temperatures and in the presence of glycerol, spectral intermediates possess very different absorption maxima as well as being much longer-lived (*35*). They are presumably structurally distinct from the intermediates at room temperature. Indeed, the cryogenic structure 3pyp also contains the flipped carbonyl (*34*) but was identified with the blue-shifted, cryogenic spectroscopic intermediate PYP_{BL} (*35*).

Entry into the Photocycle. PYP reconstituted with chemical variants of the chromophore may still enter a reversible photocycle (*36*), even though the double and triple bonds corresponding to the vinyl of the native chromophore in these variants are unable to undergo isomerization. Isomerization about the vinyl bond of the PYP chromophore is evidently not essential to entering into a photocycle. However, the variant chromophores all retain the carbonyl group and the ability to flip about the thioester bond. It appears that the photon energy absorbed by the chromophore is initially transferred into the protein by flipping the carbonyl oxygen into the very hydrophobic environment formed by several aromatic groups. In contrast to PYP, green fluorescence protein (GFP; *37*) from *Aequorea victoria* contains a chemically related chromophore and/or fluorophore (see Figure 2 of ref *26*) and efficiently fluoresces upon excitation. The corresponding carbonyl group of the GFP chromophore cannot flip since it is covalently incorporated into the imidazolone ring, derived from post-translational cyclization of the Ser65-Tyr66-Gly67 sequence of GFP. However, the phenol group could still move by isomerization about the chromophore double bond (see Figure 2 of ref *37*). Unlike PYP, GFP does not efficiently enter a photocycle (*38*). Rather, the structural flexibility to allow flipping of the carbonyl group is the key structural feature that distinguishes efficient de-excitation by a fluorescence pathway from entry into a photocycle pathway. Restricting rapid, sub-nanosecond motion of this carbonyl promotes efficient fluorescence and hinders entry to a photocycle; allowing motion shuts down the fluorescence pathway and opens that to a photocycle.

Structural Changes in the Chromophore Environment. At the proximal side, Cys69 is located in a very tight, S-shaped loop consisting of two overlapping, type III turns, spanning residues Ala67−Thr70 and Pro68−Asp71 (*26*). Four prominent negative features on the carbonyl oxygens of Ala67, Pro68, and Cys69, and the α-carbon and γ-sulfur of Cys69 appear to vary in magnitude in a correlated fashion from tens of nanoseconds to tens of microseconds. These negative features and associated, nearby positive features suggest that these tight turns undergo a series of conformational changes to accommodate isomerization of the chromophore. A recent NMR spectroscopic study also shows a significant change in the H−D exchange rate of the backbone amide hydrogen of Thr70 during the PYP photocycle (*39*).

The H-bonding network at the distal side is shown in Figure 1. The negative feature on the phenolate oxygen of the chromophore persists throughout the entire photocycle and indicates displacement from its position in the dark state. The cryogenic structure 3pyp models the phenolate oxygen at a position displaced toward the original location of the aryl moiety in its dark state (*34*). Our maps are largely consistent with this model in the earliest time range, before 16 ns. Later, two positive features denoted δ and ϵ in panels d and e of Figure 4 develop near the C_4' and C_3' atoms of the aromatic ring (but not in the plane of the ring). The feature δ starts to diminish after 2 μs, but ϵ persists until 1 ms and then moves toward Arg52. These features can most readily be interpreted as arising from new positions of the phenolate oxygen, in a mixture of two (or more) structural intermediates. These intermediates evidently have identical red-shifted absorption spectra, since the mixed structural state coexists in time with the I_1 spectroscopic state in solution, from 10 ns to 1 ms (*30*, *32*).

Negative features on the phenolate oxygen of Tyr42 and the hydroxyl oxygen of Glu46 and positive features nearby show that these groups are displaced throughout the photocycle. Positive features between Thr50 and the aryl moiety of the chromophore indicate that Thr50 moves toward the chromophore slightly in the first few nanoseconds, and moves significantly after 1 ms when the aryl moiety of the chromophore moves completely toward the solvent from its dark state position (*12*). The negative and positive features associated with motion of the guanidinium group of Arg52 that forms the lid on the chromophore pocket are largely absent until 8 ns, prominent from 4 μs to 512 μs, and very prominent thereafter until 4 ms, after which they decay. The guanidinium group of Arg52 thus appears to start moving away from the chromophore only a few nanoseconds after photon absorption. That is, the lid of the chromophore pocket begins to open long before the chromophore moves out of its pocket. Motion of the guanidinium group is correlated with motion of Thr50 to which it is H-bonded. The H-bond from the guanidinium group to the backbone carbonyl oxygen of Thr50 seems to remain undisrupted until 1 ms, when the phenolic chromophore finally pushes the guani-

dinium group to its fully open position also observed in the structure 2pyp (*12*). Significant features are observed within a few nanoseconds on atoms that are not interacting directly with the chromophore, such as those located on the guanidinium group of Arg52. This suggests that the H-bond network propagates structural signals quickly over large distances.

The strained helix C exhibits many noncanonical backbone dihedral angles in the dark state (*7*, *26*) and contains important residues involved in the distal H-bond network, Tyr42, Glu46, Thr50, and Arg52 (Figure 1). Atoms involved in backbone stabilization in helix C exhibit significant motion during the photocycle, as indicated by significant features on the main chain carbonyl oxygens and amide nitrogens, for example, of residues Ala45−Gly47. However, neither the present data nor those from a longer time scale (*12*) reveal any large-scale unfolding of PYP in the crystal, as discussed further below.

Protein Quake and Its Epicenter. The above discussion has concentrated on the most prominent structural changes, largely associated with the chromophore and its H-bonding networks. Of equal interest are those other nearby atoms or groups that do not exhibit structural changes despite the overall, light-induced protein quake in PYP, to use the graphic phrase of Frauenfelder and co-workers (*40*). Notably, the carbonyl carbon C_1 of the chromophore appears to be the epicenter of the protein quake. Unlike in real earthquakes, this epicenter is quiet; almost no electron density changes occur there throughout the photocycle (Figures 4 and 5 and the movie). As discussed above, prominent features of difference electron density originate around (but not on) the carbonyl carbon, propagate in a few nanoseconds through the thioester linkage to the proximal side of the protein backbone and through the vinyl and aryl moiety to the distal side H-bond network, and reach the gating guanidinium group of Arg52, 6−10 Å away from the epicenter, in tens of nanoseconds (Figure 4 and the movie). To visualize the overall form of this light-induced protein quake more completely, the INS procedure was repeated with a lower level of noise suppression restricted to the bulk solvent, and thus treated all difference densities in the protein region uniformly, whether close to or far from the chromophore. Exponential fitting in reciprocal space (eq 3) for the new INS maps was repeated, using the same set of relaxation rates and relative extents of photoinitiation derived before, and resulted in a second movie (data not shown). The amplitude of structural perturbation in this movie is plotted as a function of time delay t and distance to the carbonyl carbon epicenter in Figure 5. At the beginning of the photocycle, most structural changes are within 5 Å of this atom, but some longer-range structural changes 10−15 Å away from the epicenter occur very rapidly, within a few nanoseconds. Short-range structural changes decline in magnitude after 10 μs, while more changes appear at longer range, 15 Å and beyond.

Comparison with Studies in Solution. Does placing a molecule in an unusual solvent and embedding it in a crystal lattice significantly alter its structure and its functional properties? The usefulness of macromolecular crystallography rests on the fact that the answer to this question is, in general, no. However, the question must be re-examined when transient, intermediate structures are considered, in either time-resolved or trapping experiments in crystallography.

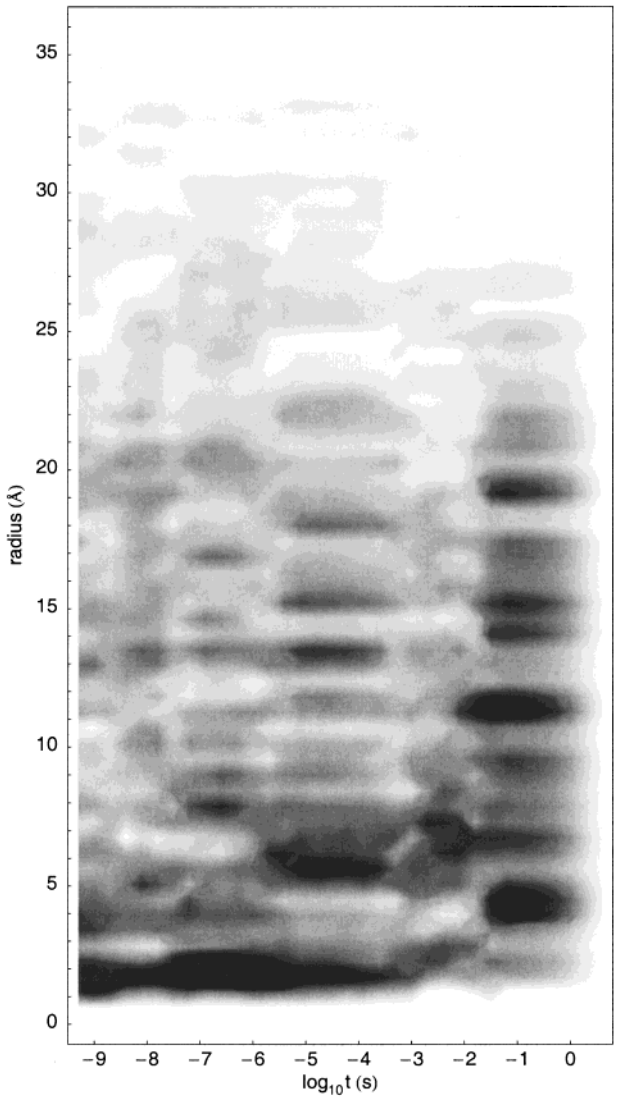

FIGURE 5: Protein quake observed during the PYP photocycle. The amplitude of light-induced structural disturbance in PYP is displayed as a function of both time delay after laser illumination and radius from the epicenter at carbonyl C_1 of the chromophore. Darker gray indicates a greater amplitude of structural disturbance, which is measured by the mean of the absolute value of large difference densities in the shell centered at the epicenter. Density values of less than 3σ were considered noise and therefore not counted in the mean, where σ is the standard deviation of the entire map.

The nature of the optical absorption spectra and the rate constants of the interconversion of the intermediates serve as sensitive probes of the structure and function of PYP. If these are significantly altered under a certain set of experimental conditions [as the spectra are, for example, in frozen solutions (*35*)], then the relevance of those conditions can be questioned. The rates of the late stages of the PYP photocycle, in which the I_1 state decays to the I_2 state and finally reverts to the dark state pG, are only modestly affected in the crystalline state. They are altered by up to a factor of 10 from their values in solution, or 1.4 kcal/mol in the free energies of activation (see Figure 9 of ref *31*; R. Kort, J. Hendriks, and K. J. Hellingwerf, unpublished results). However, there appear to be no data on the rates of the early

stages of the photocycle in the crystal, and we have therefore relied on the solution values.

Magnetic resonance data on the structure of a photostationary state in solution have revealed substantial unfolding (*41*, *42*), in contrast to crystallographic data that identified extensive tertiary structural changes but not of the magnitude that could be classed as unfolding (*12*). Under rather different conditions, the experiments are conducted and a photostationary state is populated. One interpretation is the PYP can exhibit numerous blue-shifted spectral states that are identical in optical absorption but different in structure. The states are populated to different extents depending on the exact experimental conditions, including the time of illumination, the wavelength used, the dimensions and concentration of the sample, the temperature, the pH, and whether the sample is a homogeneous solution or crystalline.

The difficulties in relating solution and crystal data are further illustrated by recent time-resolved FTIR spectroscopy results in solution of wild-type PYP, the E46Q mutant, and wild-type crystals (*43*). FTIR spectra probe the vibrational structure of a certain group or collections of similar groups. However, the spectra are not necessarily sensitive to all groups, nor do they directly reveal structure; there is no direct relation between the magnitude ΔA of the change in absorbance of an FTIR spectral feature and the spatial extent of the underlying structure change. The evolution of time-resolved FTIR spectra during the PYP photocycle differs qualitatively in solution and in crystals (see Figure 3 of ref *43*). Our results show that significant structural changes are evident from the earliest states of the photocycle in the crystal (Figure 4 and the movie), when the magnitudes of the changes in the FTIR spectra in solution (and presumably also in the crystal) are small. The structural changes in the crystal evolve in spatial extent and magnitude (Figures 4 and 5), but the magnitudes of the changes in the FTIR spectra in the crystal remain smaller than those in solution (see Figure 3 of ref *43*). Xie et al. (*43*) therefore proposed that the protein quake in solution originates late in the photocycle, upon deprotonation of Glu46. We propose here that in the crystal it originates at a very early stage of the photocycle, upon flipping of the carbonyl oxygen of the tail of the chromophore.

CONCLUSIONS

The explicit, time-dependent X-ray experiments presented here on the nanosecond to second time range differ in concept from experiments that seek to trap a high population of a candidate intermediate by either chemical or physical manipulation of the system, and then to study the trapped state in a time-independent manner (*44*). Recent examples include studies on longer-lived, candidate intermediates in the photocycle of bacteriorhodopsin [reviewed by Kuhlbrandt (*45*)] and in the catalytic mechanisms of cytochrome cd_1 nitrite reductase (*46*) and cytochrome P450 (*47*). Explicit, time-dependent experiments are advantageous for examining very short-lived intermediates with lifetimes of less than, for example, 500 μs; trapping experiments are particularly effective for longer-lived intermediates (*48*).

These data allow us to group structural elements in PYP on the basis of shared time dependence of variation in their features, and to place specific temporal and structural constraints on the determination of poorly populated, transient or mixed structural species. They also present explicit, time-resolved Laue diffraction techniques for monitoring reaction mechanisms, and compare them with trapping techniques.

ACKNOWLEDGMENT

We thank Drs. K. J. Hellingwerf, W. Hoff, M. Schmidt, and X. Yang for reading an earlier draft and stimulating discussions.

SUPPORTING INFORMATION AVAILABLE

An Argand diagram that shows the construction of the INS difference structure factor. This material is available free of charge via the Internet at http://pubs.acs.org.

REFERENCES

1. Meyer, T. E. (1985) *Biochim. Biophys. Acta 806*, 175−183.
2. Hoff, W. D., Düx, P., Hård, K., Devreese, B., Nugteren-Roodzant, I. M., Crielaard, W., Boelens, R., Kaptein, R., Van Beeumen, J., and Hellingwerf, K. J. (1994) *Biochemistry 33*, 13959−13962.
3. Baca, M., Borgstahl, G. E. O., Boissinot, M., Burke, P. M., Williams, D. R., Slater, K. A., and Getzoff, E. D. (1994) *Biochemistry 33*, 14369−14377.
4. Sprenger, W. W., Hoff, W. D., Armitage, J. P., and Hellingwerf, K. J. (1993) *J. Bacteriol. 175*, 3096−3104.
5. Pellequer, J.-L., Wager-Smith, K. A., Kay, S. A., and Getzoff, E. D. (1998) *Proc. Natl. Acad. Sci. U.S.A. 95*, 5884−5890.
6. Gu, Y.-Z., Hogenesch, J. B., and Bradfield, C. A. (2000) *Annu. Rev. Pharmacol. Toxicol. 40*, 519−561.
7. Borgstahl, G. E., Williams, D. R., and Getzoff, E. D. (1995) *Biochemistry 34*, 6278−6287.
8. Kim, M., Mathies, R. A., Hoff, W. D., and Hellingwerf, K. J. (1995) *Biochemistry 34*, 12669−12672.
9. Xie, A., Hoff, W. D., Kroon, A. R., and Hellingwerf, K. J. (1996) *Biochemistry 35*, 14671−14678.
10. Imamoto, Y., Mihara, K., Hisatomi, O., Kataoka, M., Tokunaga, F., Bojkova, N., and Yoshihara, K. (1997) *J. Biol. Chem. 272*, 12905−12908.
11. van Brederode, M. E., Gensch, T., Hoff, W. D., Hellingwerf, K. J., and Braslavsky, S. E. (1995) *Biophys. J. 68*, 1101−1109.
12. Genick, U. K., Borgstahl, G. E. O., Ng, K., Ren, Z., Pradervand, C., Burke, P. M., Šrajer, V., Teng, T.-Y., Schildkamp, W., McRee, D. E., Moffat, K., and Getzoff, E. D. (1997) *Science 275*, 1471−1475.
13. Kort, R., Vonk, H., Xu, X., Hoff, W. D., Crielaard, W., and Hellingwerf, K. J. (1996) *FEBS Lett. 382*, 73−78.
14. Stoddard, B. L. (1998) *Curr. Opin. Struct. Biol. 8*, 612−618.
15. Ren, Z., Bourgeois, D., Helliwell, J. R., Moffat, K., Šrajer, V., and Stoddard, B. L. (1999) *J. Synchrotron Radiat. 6*, 891−917.
16. Moffat, K. (1989) *Annu. Rev. Biophys. Biophys. Chem. 18*, 309−332.
17. Kort, R., Hoff, W. D., Van West, M., Kroon, A. R., Hoffer, S. M., Vlieg, K. H., Crielaard, W., Van Beeumen, J. J., and Hellingwerf, K. J. (1996) *EMBO J. 15*, 3209−3218.
18. Imamoto, Y., Ito, T., Kataoka, M., and Tokunaga, F. (1995) *FEBS Lett. 374*, 157−160.
19. McRee, D. E., Meyer, T. E., Cusanovich, M. A., Parge, H. E., and Getzoff, E. D. (1986) *J. Biol. Chem. 261*, 13850−13851.
20. Wulff, M., Schotte, F., Naylor, G., Bourgeois, D., Moffat, K., and Mourou, G. (1997) *Nucl. Instrum. Methods Phys. Res. A398*, 69−84.
21. Bourgeois, D., Ursby, T., Wulff, M., Pradervand, C., LeGrand, A., Schildkamp, W., Labouré, S., Šrajer, V., Teng, T. Y., Roth, M., and Moffat, K. (1996) *J. Synchrotron Radiat. 3*, 65−74.

22. Ren, Z., and Moffat, K. (1995) *J. Appl. Crystallogr. 28*, 461−481.
23. Ren, Z., and Moffat, K. (1995) *J. Appl. Crystallogr. 28*, 482−493.
24. Ursby, T., and Bourgeois, D. (1997) *Acta Crystallogr. A53*, 564−575.
25. Tulinsky, A. (1985) *Methods Enzymol. 115*, 77−89.
26. Perman, B., Šrajer, V., Ren, Z., Teng, T.-Y., Pradervand, C., Ursby, T., Bourgeois, D., Schotte, F., Wulff, M., Kort, R., Hellingwerf, K., and Moffat, K. (1998) *Science 279*, 1946−1950.
27. Henderson, R., and Moffat, K. (1971) *Acta Crystallogr. B27*, 1414−1420.
28. Cornish-Bowden, A. (1995) *Fundamentals of Enzyme Kinetics*, Portland Press, London.
29. More, J. J. (1978) in *Lecture Notes in Mathematics* (Watson, G. A., Ed.) No. 630, Springer-Verlag, Berlin.
30. Hoff, W. D., van Stokkum, I. H. M., van Ramesdonk, H. J., van Brederode, M. E., Brouwer, A. M., Fitch, J. C., Meyer, T. E., van Grondelle, R., and Hellingwerf, K. J. (1994) *Biophys. J. 67*, 1691−1705.
31. Ng, K., Getzoff, E. D., and Moffat, K. (1995) *Biochemistry 34*, 879−890.
32. Meyer, T. E., Tollin, G., Hazzard, J. H., and Cusanovich, M. A. (1989) *Biophys. J. 56*, 559−564.
33. Meyer, T. E., Tollin, G., Cusanovich, M. A., Perman, B., Wulff, M., Hellingwerf, K., and Moffat, K. (1998) *Science 281*, 1964.
34. Genick, U. K., Soltis, S. M., Kuhn, P., Canestrelli, I. L., and Getzoff, E. D. (1998) *Nature 392*, 206−209.
35. Imamoto, Y., Kataoka, M., and Tokunaga, F. (1996) *Biochemistry 35*, 14047−14053.
36. Cordfunke, R., Kort, R., Pierik, A., Gobets, B., Koomen, G.-J., Verhoeven, J. W., and Hellingwerf, K. J. (1998) *Proc. Natl. Acad. Sci. U.S.A. 95*, 7396−7401.
37. Phillips, G. N., Jr. (1997) *Curr. Opin. Struct. Biol. 7*, 821−827.
38. van Thor, J. J., Pierik, A. J., Nugteren-Roodzant, I., Xie, A., and Hellingwerf, K. J. (1998) *Biochemistry 37*, 16915−16921.
39. Craven, J. C., Derix, N. M., Hendriks, J., Boelens, R., Hellingwerf, K. J., and Kaptein, R. (2000) *Biochemistry 39*, 14392−14399.
40. Ansari, A., Berendzen, J., Bowne, S. F., Frauenfelder, H., Iben, I. E. T., Sauke, T. B., Shyamsunder, E., and Young, R. D. (1985) *Proc. Natl. Acad. Sci. U.S.A. 82*, 5000−5004.
41. Rubinstenn, G., Vuister, G. W., Mulder, F. A. A., Düx, P. E., Boelens, R., Hellingwerf, K. J., and Kaptein, R. (1998) *Nat. Struct. Biol. 5*, 568−570.
42. Rubinstenn, G., Vuister, G. W., Zwanenburg, N., Hellingwerf, K. J., Boelens, R., and Kaptein, R. (1999) *J. Magn. Reson. 137*, 443−447.
43. Xie, A., Kelemen, L., Hendriks, J., White, B. J., Hellingwerf, K. J., and Hoff, W. D. (2001) *Biochemistry 40*, 1510−1517.
44. Moffat, K., and Henderson, R. (1995) *Curr. Opin. Struct. Biol. 5*, 656−663.
45. Kuhlbrandt, W. (2000) *Nature 406*, 569−570.
46. Williams, P. A., Fülop, V., Garman, E. F., Saunders, N. F. W., Ferguson, S. J., and Hajdu, J. (1997) *Nature 389*, 406−412.
47. Schlichting, I., Berendzen, J., Chu, K., Stock, A. M., Maves, S. A., Benson, D. E., Sweet, R. M., Ringe, D., Petsko, G. A., and Sligar, S. G. (2000) *Science 287*, 1615−1622.
48. Moffat, K. (2001) *Chem. Rev. 101*, 1569−1581.
49. Carson, M. (1997) *Methods Enzymol. 277*, 493−505.
50. Ujj, L., Devanathan, S., Meyer, T. E., Cusanovich, M. A., Tollin, G., and Atkinson, G. H. (1998) *Biophys. J. 75*, 406−412.
51. Devanathan, S., Pacheco, A., Ujj, L., Cusanovich, M., Tollin, G., Lin, S., and Woodbury, N. (1999) *Biophys. J. 77*, 1017−1023.
52. Šrajer, V., Ren, Z., Teng, T.-Y., Schmidt, M., Ursby, T., Bourgeois, D., Pradervand, C., Schildkamp, W., Wulff, M., and Moffat, K. (2001) *Biochemistry 40*, 13802−13815.

BI0107142